

TESS search for substellar companions through pulsation timing of δ Scuti stars

I. Discovery of companions around Chang 134 and V393 Car

V. Vaulato^{*1}, V. Nascimbeni^{**2}, and G. Piotto^{1,2}

¹ Dipartimento di Fisica e Astronomia, Università degli Studi di Padova, Vicolo dell'Osservatorio 3, 35122 Padova, Italy

² INAF – Osservatorio Astronomico di Padova, Vicolo dell'Osservatorio 5, 35122 Padova, Italy

Accepted: 2 September 2022

ABSTRACT

Early-type main-sequence pulsating stars such as δ Scuti variables are one of the least explored class of targets in the search for exoplanets. Pulsation timing (PT) is an alternative technique to the most effective search methods. It exploits the light-travel-time effect (LTTE) to infer the presence of additional massive bodies around a pulsating star by measuring a periodic phase modulation of its signal. PT has been extremely successful in discovering and characterizing stellar binaries when it was applied to high-precision light curves over long temporal baselines, such as those delivered by the Kepler mission. In favorable conditions, the sensitivity of PT can reach the planetary-mass regime; one such candidate has already been claimed. The advent of TESS, with its nearly full-sky coverage and the availability of full-frame images, opens a great opportunity to expand this field of research. In this work, we present a pilot study aimed to understand the potential of PT as applied to TESS data, which are considerably different from Kepler data in terms of photometric noise, sampling cadence, and temporal baseline. We focused on the most favorable class of δ Scuti, that is, those showing strong pulsations and very simple frequency spectra. After the development of a customized pipeline, we were able to detect candidate companions for two targets in the (sub-)stellar mass regime: Chang 134 ($43 \pm 5 M_{\text{jup}}$, $P \simeq 82$ d) and V393 Car ($\geq 100 M_{\text{jup}}$, $P \gtrsim 700$ d). Our results also highlight the limiting factors of this technique and the importance of an accurate absolute time calibration for future missions such as PLATO.

Key words. Stars: oscillations – Stars: variables: delta Scuti – Techniques: photometric – Methods: data analysis – Planetary systems – Planets and satellites: detection – binaries: general

1. Introduction

Since the pioneering detections of 51 Peg b, the first exoplanet orbiting a solar-type star (Mayor & Queloz 1995), and HD209458b, the first transiting hot Jupiter (Henry et al. 2000; Charbonneau et al. 2000), contemporary exoplanetary research has mostly focused on late-type (FGKM) main-sequence hosts. This is not just because of the interesting analogies with our own Solar System, but also because these stars are particularly suited for the most fruitful detection techniques in terms of discoveries: radial velocities (RV) and transits. These two techniques are hampered by the presence of stellar activity and pulsations, making the detection and characterization of planets around very young, evolved, or early-type stars extremely challenging. Along these lines, the somewhat standard road to discovery has become the photometric detection of transit-like signals, followed by an RV monitoring to confirm the planetary nature of the candidate and to measure its mass.

The vast majority of transiting planets known today have been discovered by dedicated space-based telescopes: starting with the pioneering work of the CoRoT satellite (2006-2013; built by an international consortium led by CNES; Auvergne et al. 2009), which was followed by the Kepler mission by NASA (2009-2014; Borucki et al. 2010). Kepler was stopped because

of a technical failure and was then restored for a second-phase observing program called K2 (2014-2018; Howell et al. 2014). Finally, the advent of the NASA *Transiting Exoplanet Survey Satellite* (TESS; Ricker et al. 2015), launched in 2018 and currently operating, doubled the number of known candidate exoplanets by starting the first all-sky space-based transit survey. TESS is optimized to search for Earth- to Neptune-sized planets transiting bright and nearby main-sequence stars with a particular focus on cool, red dwarfs (K and M) because their smaller radii and lower masses make the transit and RV signals much stronger. TESS objects of interest are three magnitudes brighter than those of Kepler on average (Barclay et al. 2018), enabling an easier and more effective spectroscopic follow-up analysis. Most importantly in this context, and unlike its predecessors, TESS has the capability to download photometric data not only for a limited sample of preselected targets, but also for virtually any other bright star in the sky, although at a longer cadence with respect to the core sample. This is made possible by the availability of full-frame images (FFIs), originally downloaded every 30 minutes, and since sector 27, at a 10-minute cadence. FFI photometry opened a vast array of opportunities in many astrophysical fields, including extending the search for planets to a wider range in the stellar parameter space (Montalto et al. 2020; Nardiello et al. 2019).

Several alternative detection techniques have been proposed and implemented to search for exoplanets around stars other than

* E-mail: valentina.vaulato@unige.ch

** E-mail: valerio.nascimbeni@inaf.it

solar-type or M dwarfs, or in different Galactic environments. A-type stars, in particular, are one of the least explored class of planet-hosting stars. Of more than 5 000 confirmed planets with known mass and/or radius listed in the NASA Exoplanet Archive, only 22 are hosted by 21 main-sequence stars earlier than the F0V spectral type ($T_{\text{eff}} \geq 7220$ K; [Pecaut & Mamajek 2013](#)). With only four exceptions coming from direct imaging surveys, they were all detected through the transit technique (3 by HAT-Net, 3 by WASP, 5 by KELT, 2 by MASCARA, 3 by Kepler, 2 by TESS) and were confirmed by means of spectral tomography ([Collier Cameron et al. 2010](#)) and/or statistical validation techniques because classical RV measurements are usually not effective on such stars, whose spectral lines are few and Doppler broadened by their very high rotational velocities ($v \sin i \sim 100$ km/s; [Rainer et al. 2021](#)).

Only three of the hosts described above are confirmed or suspected δ Scuti variables, that is, population I pulsators located in the classical Cepheid instability strip ([Bowman & Kurtz 2018](#); [Guzik 2021](#) and references therein): WASP-33b ([Herrero et al. 2011](#)), HAT-P-57b ([Hartman et al. 2015](#)), and WASP-167b = KELT-13b ([Temple et al. 2017](#)). Because $\sim 50\%$ of the stars in this region of the parameter space are expected to show δ Scuti pulsations to some extent ([Bowman 2017](#)), some astrophysical reason must explain the lack of planets around δ Scuti stars, and/or a strong observational selection effect is at play. The latter explanation is likely true, as the stellar pulsation pattern is known to limit the efficiency of transit-search algorithms even after they are filtered in the frequency domain by sophisticated techniques ([Ahlers et al. 2019](#); [Hey et al. 2021](#)).

In this context, the pulsation timing technique (PT; [Hermes 2018](#)) is a completely independent method for detecting massive companions around stars showing coherent and well-detectable pulsations, such as δ Scuti stars, pulsating white dwarfs, or hot subdwarfs. The underlying physical principle is the so-called light-travel-time effect (LTTE) that was first discussed in detail by [Irwin \(1952\)](#): Because the speed of light c is finite, the motion of the target along the line of sight will translate into a phase shift of any periodic astrophysical signal originating from the star, including pulsations. The arrival times of the signals can then be compared with those predicted by a linear ephemeris (implying a constant periodicity $dP/dt = 0$) by computing the so-called O–C diagram (observed – calculated; [Sterken 2005](#)). Any deviation from a strict periodicity $dP/dt \neq 0$ (assuming that the pulsation themselves are intrinsically stable) would then reveal itself as a nonzero second derivative in the O–C diagram (see [Sec. 3](#) for details). The LTTE signal from a single, massive perturber on a Keplerian orbit is formally analogous to an RV curve having half of the eccentricity e and the argument of the periastris ω decreased by $\pi/2$ ([Irwin 1952](#)); if the full shape of the LTTE signal is retrieved, then the orbital period P , the minimum mass $M \sin i$, and other orbital elements of the perturber can be reliably measured. The PT approach shares some similarities with the astrometric method ([Black & Scargle 1982](#)) in that it measures the displacement of the target star with respect to an inertial rest frame, but projected along the line of sight rather than on the sky plane. Notably, also the underlying selection effects are similar because both methods are more sensitive to massive bodies at large star-planet separations. PT therefore probes a region of the parameter space that is complementary to the space that is investigated by transits and RVs, which are more sensitive to close-in perturbers ([Sozzetti 2005](#)).

The PT technique requires photometric data spanning a temporal baseline that is long enough to sample the orbital period of the perturber and a signal-to-noise ratio (S/N) high enough to

constrain the phase shift of the oscillations to a level comparable to the expected LTTE amplitude¹. The main pulsation modes of the star have to be individually identified and measured on the Fourier spectrum of the light curve, implying that continuous time series spanning at least ~ 10 days are mandatory to achieve the needed resolution in the frequency space (~ 0.1 cycles/day) when dealing with the harmonic content of typical δ Scuti stars ([Murphy et al. 2014](#)). This is the main reason why sparse sampling imposed by the day-night cycle is the main limiting factor of ground-based observations. Targets with an extremely simple harmonic content, such as pseudo-sinusoidal pulsators, represent an exception, and a few pioneering results were published by analyzing ground-based data ([Paparo et al. 1988](#); [Barlow et al. 2011b](#)). Interestingly, the latter claim was subsequently confirmed by an independent RV follow-up, demonstrating the reliability of this technique ([Barlow et al. 2011a](#)).

The full power of the PT technique, however, revealed itself when the nearly uninterrupted 4 yr baseline of Kepler photometry was exploited. Some works ([Shibahashi & Kurtz 2012](#); [Murphy et al. 2014](#); [Shibahashi et al. 2015](#); [Murphy & Shibahashi 2015](#); [Murphy et al. 2018, 2020](#)), although they focused on the detection and characterization of stellar-mass companions, demonstrated that under favorable assumptions, even LTTE signals from planetary-mass companions ($\lesssim 13 M_{\text{jup}}$) are in principle detectable through space-based photometry ([Murphy et al. 2014](#)). [Murphy et al. \(2016\)](#) presented the PT detection of a massive planetary candidate for the first time ($11.8 \pm 0.7 M_{\text{jup}}$, $P = 840 \pm 20$ d). This candidate orbits a metal-poor δ Scuti star (KIC 7917485). Together with the discovery by [Silvotti et al. \(2007\)](#) of a giant planet around the hot subdwarf B star V391 Peg, these are the only PT discoveries of planetary-mass objects published so far. It should be noted, however, that a follow-up paper on V391 Peg with new data ([Silvotti et al. 2018](#)) failed to fully reproduce the previous claim, probably due to non-linear interactions between pulsation modes (see also [Bowman et al. 2021](#)). This acts as a caution.

While several studies of δ Scuti stars have been published that exploited TESS short-cadence data ([Antoci et al. 2019](#); [Hasanzadeh et al. 2021](#); [Southworth 2021](#) for a review), none of them applied the PT technique. The goal of this paper is to focus on the PT analysis of a small sample of particularly suited targets observed by TESS at short cadence as a pilot study for the exploitation of TESS (and, later on, PLATO) data on a larger scale. In [Section 2](#) we describe how our targets were identified and how their relevant stellar parameters were collected. In [Section 3](#) we summarize all the steps of our data analysis, starting from the filtering of raw light curves through the harmonic analysis to measure the phase shifts as a function of time. We determine the best-fit orbital solutions through an LTTE model in [Section 4](#) and discuss the results in [Section 5](#).

2. Target selection and characterization

The vast majority of targets observed by TESS at short and ultra-short photometric cadence (120 and 20 s, respectively) are FGKM dwarfs selected for the core transit-search survey, drawn from the so-called candidate target list (CTL; [Fausnaugh et al. 2021](#)). However, stars of different spectral types, including pulsating variables, are ingested mostly from GI/DDT proposals or from the TESS Asteroseismic Science Operation Cen-

¹ As a comparison, the LTTE effect induced by the orbital motion of Jupiter around the Sun, as seen edge-on, is ~ 10 s ([Schneider 2005](#)), with a period of ~ 12 years. See also [Sec. 5](#).

Table 1. Adopted stellar parameters and other basic information for Chang 134 (second and third columns) and V393 Car (fourth and fifth columns). See Section 2 for details.

parameter	Chang 134		V393 Car	
	value	source (& ref.)	value	source (& ref.)
TIC (ID)	431589510	TICv8 (A)	364399376	TICv8 (A)
TYC (ID)	9158-919-1	Tycho-2 (B)	8911-2754-1	Tycho-2 (B)
HD (ID)	—	—	66260	Simbad (C)
2MASS (ID)	J03224585-7237459	2MASS (D)	J07590267-6135009	2MASS (D)
R. A. [deg]	50.69114	Gaia EDR3 (E)	119.76113	Gaia EDR3 (E)
declination [deg]	-72.62943	Gaia EDR3 (E)	-61.58361	Gaia EDR3 (E)
parallax [mas]	0.75 ± 0.11	Gaia EDR3 (E)	5.00 ± 0.10	Gaia EDR3 (E)
distance [pc]	1090 ± 120	Gaia EDR3 (F)	199 ± 5	Gaia EDR3 (F)
T (mag)	11.89 ± 0.01	TICv8 (A)	7.185 ± 0.007	TICv8 (A)
B (mag)	12.35 ± 0.11	Tycho-2 (B)	7.76 ± 0.01	Tycho-2 (B)
V (mag)	12.33 ± 0.17	Tycho-2 (B)	7.46 ± 0.01	Tycho-2 (B)
J (mag)	11.40 ± 0.02	2MASS (D)	6.84 ± 0.02	2MASS (D)
H (mag)	11.29 ± 0.02	2MASS (D)	6.75 ± 0.06	2MASS (D)
K_s (mag)	11.23 ± 0.02	2MASS (D)	6.68 ± 0.02	2MASS (D)
T_{eff} [K]	7200 ± 300	seismic (G)	7400 ± 200	seismic (G)
"	7281 ± 170	Gaia DR2 (H)	7040 ± 280	Gaia DR2 (H)
L_{\star}/L_{\odot}	—	—	27.44 ± 0.32	Gaia DR2 (H)
M_{\star}/M_{\odot}	1.38 ± 0.03	StarHorse (I)	2.02 ± 0.10	StarHorse (J)
R_{\star}/R_{\odot}	—	—	3.52 ± 0.29	Gaia DR2 (H)
$\log g_{\star}$ [cgs]	4.04	seismic (G)	3.58	seismic (G)

Notes. References: A) TESS Input Catalog Version 8 (Stassun et al. 2019); B) Tycho-2 (Høg et al. 2000); C) Simbad data base, (Wenger et al. 2000); D) Two Micron All Sky Survey (2MASS, Cutri et al. 2003); E) Gaia Early Data Release 3 (EDR3, Gaia Collaboration et al. 2021); F) Bailer-Jones et al. (2021); G) Barceló Forteza et al. (2020); H) Gaia Data Release 2 (DR2, Gaia Collaboration et al. 2018); I) Queiroz et al. (2020); J) Anders et al. (2022).

ter (TASOC²), which provides the TESS Asteroseismic Science Consortium (TASC) with an asteroseismological database of the mission (Schofield et al. 2019).

In order to select our targets, we chose the catalog compiled by Chang et al. (2013) as a starting point. This catalog lists a sample of 1,578 δ Scuti stars that were identified at high confidence level by several previous surveys. We cross-matched this catalog with the TESS CTL tables for sectors from 1 to 42 included to obtain only δ Scuti stars that were observed by TESS at two-minute cadence. As an additional constraint, we further restricted our sample by 1) requiring a minimum data coverage of at least seven TESS sectors, not necessarily contiguous, to build $O-C$ diagrams with a number of points and a temporal baseline long enough to detect LTTE signals at an approximately one-year timescale (see Section 4); 2) selecting targets brighter than $T = 12$ in the TESS photometric system, to avoid being limited by photon and background noise; and 3) excluding all the stars that have been identified as binaries in the Chang et al. (2013) catalog. These additional constraints are justified by the nature of this study, which is not focused on a complete sample, but is rather intended as a pilot study to investigate the limiting factors of TESS (especially due the systematic errors) on a very small sample of the most favorable targets.

The final output of this selection process is a short list of 12 targets, which were then individually examined both through a literature search and by inspecting their TESS light curves. In particular, we confirmed that all of them are actually δ Scuti pulsators and carried out a preliminary harmonic analysis on them by computing the generalized Lomb-Scargle periodogram (GLS;

Zechmeister & Kürster 2018) of a single sector with the same algorithms as described in Section 3. While most targets are classical δ Scuti stars showing small-amplitude (~ 0.01 - 0.03 mag) pulsations and a complex pattern of different modes in the frequency domain, two of them stand out as high-amplitude pulsators (≥ 0.1 mag) with a particularly clean periodogram, in which most of the signal is due to a single, well-defined pulsation mode and its harmonics (Fig. 1, 2): hereafter we refer to them as Chang 134 (from its ID number in the Chang et al. 2013 catalog) and V393 Carinae. This combination of a large pulsation amplitude and a very simple and coherent frequency pattern makes these targets well suited for a precise timing analysis, especially for our pilot study. For this reason, we focused this analysis on them and set aside the other targets (five of which are multi-mode pulsators, but with modes that are easy to identify) for the next paper of the series. A short review of the available scientific literature is given in the following subsections, and the basic astrophysical parameters of the two targets are reported in Table 1. It is worth mentioning that both our targets could fit the high-amplitude δ Scuti subclass (HADS; Breger 2000; Antoci et al. 2019), which is characterized by large-amplitude pulsations, low rotational velocities, and time-domain spectra that are dominated by radial modes. We did not attempt to perform a detailed identification of their pulsation modes, however, because our work is focused on a dynamical technique (where the pulsation pattern is exploited just as a coherent astrophysical clock) rather than on stellar physics.

² <https://tasoc.dk>

2.1. Chang 134 = TYC 9158-919-1

Chang 134, also known as TYC 9158-919-1 or TIC 431589510, was first identified as a variable star by ASAS (Pojmanski 2002) and classified as a generic δ Scuti star (DSCT variability class). No targeted follow-up study on it has been published since 2002. An asteroseismological measurement of $\log(g)$ and T_{eff} was included in the catalog by Barceló Forteza et al. (2020) through the ν_{max} seismic index extracted from the TESS light curves in an automated fashion. All the astrophysical parameters we collected are reported in the second and third columns of Table 1.

The PT technique, just like astrometry or RVs, cannot directly infer the mass of perturbing body, but rather its ratio m_p/M_\star with the stellar mass. The latter is needed at the analysis stage (Section 4) to properly interpret our results for the two targets. For Chang 134, an estimate of stellar mass ($M_\star = 1.40 \pm 0.16 M_\odot$) and age was first published in the catalog by Mints & Hekker (2017) using UniDAM models, but without taking advantage of spectroscopic data or Gaia parallaxes, which were not available at that time. Later, Chang 134 was included in the large-scale analysis by Queiroz et al. (2020), combining high-resolution spectra from the APOGEE-2 survey DR16 with broadband photometric data taken from different sources and Gaia DR2 distances. Stellar parameters are derived as the posterior distribution returned by the Bayesian isochrone-fitting code StarHorse (Queiroz et al. 2018). The stellar mass reported for Chang 134 is $M_\star = 1.38 \pm 0.03 M_\odot$, where the central value is the 50th percentile of the StarHorse posterior distribution, while the symmetrized uncertainty is calculated as the half-difference between the 84th and the 16th percentiles of the same distribution.

2.2. V393 Carinae = HD 66260

Unlike Chang 134, the much brighter V393 Car (also known as HD 66260 or TIC 364399376) has been the subject of several targeted studies. It was first discovered as a variable star and classified as a δ Scuti radial pulsator by Helt (1984). Balona & Evers (1999) found in a more detailed analysis that the dominant mode is rather nonradial; the debate of this point is still ongoing. A first claim of change in the period of the main pulsation mode appeared in Garcia et al. (2001), who measured a 7.18-minute discrepancy with respect to the ephemeris by Helt (1984). Interestingly, further ground-based photometric follow-up by Axelsen (2014) retrieved the very same period of Helt (1984) within 0.33 s, and found no conclusive evidence of additional overtones. The present work therefore also represents an opportunity to confirm or disprove the claimed period change, and to determine whether it is caused by a secular or an oscillating term.

A measurement of ν_{max} , $\log(g)$, T_{eff} was listed by for Chang 134 by Barceló Forteza et al. (2020). Unfortunately, V393 Car is missing from the Queiroz et al. (2020) catalog, but is listed in the Anders et al. (2022) catalog, which applied StarHorse on the Gaia EDR3 photometric and astrometric measurements, yielding $M_\star = 2.02 \pm 0.10 M_\odot$ for this target. As accurate stellar parameters of V393 Car derived from spectroscopy are lacking in the literature, we attempted to obtain an independent estimate of the stellar mass as a crosscheck by applying the empirical relations derived by Moya et al. (2018) as a function of other stellar parameters. In particular, we exploited the relation

$$\log_{10}(M_\star) = -a + b T_{\text{eff}} + c \log_{10}(L_\star), \quad (1)$$

where $a = -0.119 \pm 0.003$, $b = 2.14 \times 10^{-5} \pm 5 \times 10^{-7}$ and $c = 0.1837 \pm 0.0011$ are the coefficients calculated by Moya et al. (2018). This relation is valid within the range of temperatures $4780 \leq T_{\text{eff}} \leq 10990$ K. Adopting T_{eff} from the seismic value given by Barceló Forteza et al. (2020) and L_\star from the Gaia DR2 catalog³, and propagating the errors, we computed a stellar mass $M_\star = 1.98 \pm 0.17 M_\odot$ for V393 Car, which is perfectly consistent with the previous value. We therefore adopt the $M_\star = 2.02 \pm 0.10 M_\odot$ estimate from Anders et al. (2022) in the subsequent analysis.

We are aware that a detailed asteroseismic analysis performed on all the available TESS light curves would likely yield much more accurate fundamental parameters for both our targets (Hasanzadeh et al. 2021). However, since an error of about 5% on stellar mass will not be the dominant source of uncertainty in our final parameters (as we discuss in Section 4), an analysis like this is beyond the scope of our work.

2.3. TESS light curves

Chang 134 and V393 Car were both observed by TESS in two-minute cadence mode. At the time when our analysis started, Chang 134 was observed in 9 nonconsecutive sectors (1-2-3-6-13-27-28-29-36) between July 2018 and March 2021. V393 Car was observed in 14 nonconsecutive sectors (1-4-7-8-10-11-27-28-31-34-35-36-37-38) between July 2018 and April 2021. All the photometric data analyzed in this work were processed and extracted from the raw data by the Science Processing Operations Center (SPOC) pipeline (Jenkins et al. 2016) and are publicly available on the Mikulski Archive for Space Telescopes (MAST⁴). Specifically, we built the light curves for our analysis by extracting the stellar flux from the pre-search data conditioning simple aperture photometry column (PDCSAP; Smith et al. 2012; Stumpe et al. 2012) because it results in cleaner time series since systematic long-term trends are removed.

3. Harmonic analysis

Our approach to data analysis is based on the fit of sums of harmonic functions to preselected segments of our light curves in the form

$$\sum_i f(A_i, P_i, \phi_i) = \sum_i A_i \times \cos\left(\frac{2\pi t}{P_i} + 2\pi\phi_i\right), \quad (2)$$

where A_i is the amplitude, P_i the period, and ϕ_i the phase of each component normalized between 0 and 1. The phase of the signal at the dominant pulsation mode ϕ_0 is then retrieved for each segment, giving the so-called phase shift $\phi_0(t)$ as a function of time. From this quantity, the usual $O-C$ diagram in time units can be computed in a straightforward way by just multiplying the phase shift by the pulsation period P_0 .

We developed an independent pipeline to perform all the needed tasks from the raw light curves down to the final $O-C$ diagram. Its flow chart (described in the following sections) is

³ Unfortunately, the stellar parameters reported for V393 Car by Gaia DR3 (Gaia Collaboration et al. 2022) are highly discrepant with each other and associated with unreasonably small errors, possibly because the pipeline is unable to deal with a pulsating star. We therefore adopted the DR2 values for consistency.

⁴ <https://mast.stsci.edu/portal/Mashup/Clients/Mast/Portal.html>

conceptually similar to the phase modulation (PM) method described by Murphy et al. (2014), with some substantial differences, in particular, in how the actual fit is performed, that is, through a Markov chain Monte Carlo (MCMC) analysis in our case rather than with a simple least-squares algorithm. Most of our processing steps were implemented by scripting and modifying routines from the VARTOOLS code version 1.39⁵ released by Hartman & Bakos (2016), to which we refer for a more in-depth description of the individual algorithms.

3.1. Light curve preconditioning

We started our process by downloading TESS SPOC light curves of our targets from the MAST archive for each observing sector (23 combined sectors). Each data point was sampled every two minutes as a default for short-cadence observations.

As a first step, we discarded all data points flagged as bad, that is, with a quality factor $q \neq 0$ (QUALITY column). We then extracted the time column TIME from each FITS file and converted it into the BJD_{TDB} standard (Eastman et al. 2010). Finally, we extracted the PDCSAP_FLUX column and its associated error PDCSAP_FLUX_ERR and converted them into the magnitude system. The choice of PDCSAP over SAP is justified by our need that systematic errors, especially those manifesting themselves as long-term trends, are corrected for as much as possible to avoid unnecessary noise on our periodograms. As our analysis is focused on retrieving the phase of the pulsation signal, we are not concerned by any small perturbation in the amplitudes that might be introduced by the PDCSAP processing (Cui et al. 2019). In order to filter out the most obvious outliers that survived the $q = 0$ selection, we carried out an iterative clipping at 15σ with respect to the mean. This specific threshold was empirically set by confirming that the shape of the main pulsation mode was left unchanged.

The final step of our preconditioning recipe was to split the light curves from each sector into smaller chunks that were individually analyzed later to become single points in the $O - C$ diagram. Working on continuous segments, about 10 days has been shown to be a reasonable compromise between the need of getting 1) a frequency resolution that is high enough to reliably measure the phases of the individual pulsation modes and 2) a time resolution on the $O - C$ diagram as low as possible (Murphy et al. 2014). Because for most TESS sectors the only significant interruption is the one-day central gap to allow the data downlink toward Earth at each perigee of the spacecraft, we chose that gap as a natural boundary and split each sector accordingly into two mostly continuous segments of about 14 days each, to which we refer hereafter as “orbits”. We are therefore left with 18 orbits for Chang 134 and 28 orbits for V393 Car. Each orbit was individually normalized to unit flux (and magnitude zero) before we continued to the next stages.

3.2. Frequency identification

In order to identify the most significant pulsation modes of our targets we made use of the Generalized Lomb-Scargle periodogram (GLS, Zechmeister & Kürster 2018), an improved version of the Lomb-Scargle periodogram (LS, VanderPlas 2018) which is less sensitive to aliasing and returns more accurate frequencies. Because we searched for LTTE effects, all the frequencies might in principle be slightly varying as a function of time

⁵ <https://www.astro.princeton.edu/~jhartman/vartools.html>

due to the phase shift itself. At this stage, we therefore need to calculate the average value over the full span of our observations for each frequency. This can be accomplished by stitching all the normalized orbits into a single light curve and running GLS on it. We limited our search from 1 to 50 cycles per day, thus including the typical frequency range of δ Scuti modes (Balona & Dziembowski 2011) and being well within the Nyquist limit for our sampling rate (~ 360 cycles per day). The output are two periodograms for Chang 134 and V393 Car that are visually similar to those shown in Fig. 1 and 2, but with a much higher S/N. In order to improve the estimate of the pulsation frequencies, the light curve is usually fitted by a multisinusoidal function using the periodogram peaks as a starting point (Silvotti et al. 2018). In our case, however, this additional step is not essential given the extremely high S/N of our data.

By identifying the strongest frequencies ν_i (and corresponding periods P_i) as the most prominent peaks in the periodogram, we found one dominant frequency for Chang 124 that was followed by its multiple integer harmonics, sorted hereafter by decreasing GLS power,

$$\begin{cases} P_0 = 0.12942447 \text{ d} \\ P_1 = 0.06471223 \text{ d} \\ P_2 = 0.04314149 \text{ d} \end{cases} \quad \begin{cases} \nu_0 = 7.72651415 \text{ d}^{-1} \\ \nu_1 = 15.4530283 \text{ d}^{-1} \\ \nu_2 = 23.1795424 \text{ d}^{-1} \end{cases}, \quad (3)$$

and in the same way for V393 Car,

$$\begin{cases} P_0 = 0.14129519 \text{ d} \\ P_1 = 0.07064759 \text{ d} \\ P_2 = 0.04709840 \text{ d} \end{cases} \quad \begin{cases} \nu_0 = 7.07738170 \text{ d}^{-1} \\ \nu_1 = 14.1547634 \text{ d}^{-1} \\ \nu_2 = 21.2321451 \text{ d}^{-1} \end{cases}. \quad (4)$$

A complete list of all the significant frequencies detected for Chang 134 and V393 Car can be found in Table B.1 and B.2, respectively.

For both stars, we obtained $\nu_1 = 2\nu_0$ and $\nu_2 = 3\nu_0$, that is, the three most prominent frequencies are the second and third harmonics of the main pulsation mode. Chang 134 does not show any significant peak outside the harmonic series of ν_0 . The GLS power of the strongest peak for V393 Car outside the harmonics of ν_0 (at $\sim 12.58288 \text{ d}^{-1}$) is three orders of magnitude smaller than the main mode. While irrelevant for our analysis due to its weakness, we note that this minor peak, detected at very high confidence in the TESS data, confirms the presence of an additional pulsation mode at 12.58 or 13.58 cycles per day claimed by Helt (1984) that was never confirmed by subsequent works (Garcia et al. 2001; Axelsen 2014). The very clean window function of the TESS data enables us to state that 13.58 was just a one-day alias of the real peak at 12.58 cycles per day.

3.3. Harmonic fit

After the average frequencies $\nu_i = 2\pi/P_i$ of the most powerful pulsation modes were identified, we proceeded to fit a harmonic series in the form of Eq. 2 to our light curves. As several TESS orbits are affected by long-term systematic errors even after the PDCSAP treatment (on a timescale of typically days to weeks), we added a polynomial term as a function of time to our model to mitigate their impact. After some trial and error, we concluded that a polynomial of order 2 (i.e., a quadratic baseline) is enough to provide us with an accurate fit. The full model M we fit is therefore

$$M = b_0 + b_1(t - t_m) + b_2(t - t_m)^2 + \sum_{i=0}^{N-1} f_i(A_i, P_i, \phi_i), \quad (5)$$

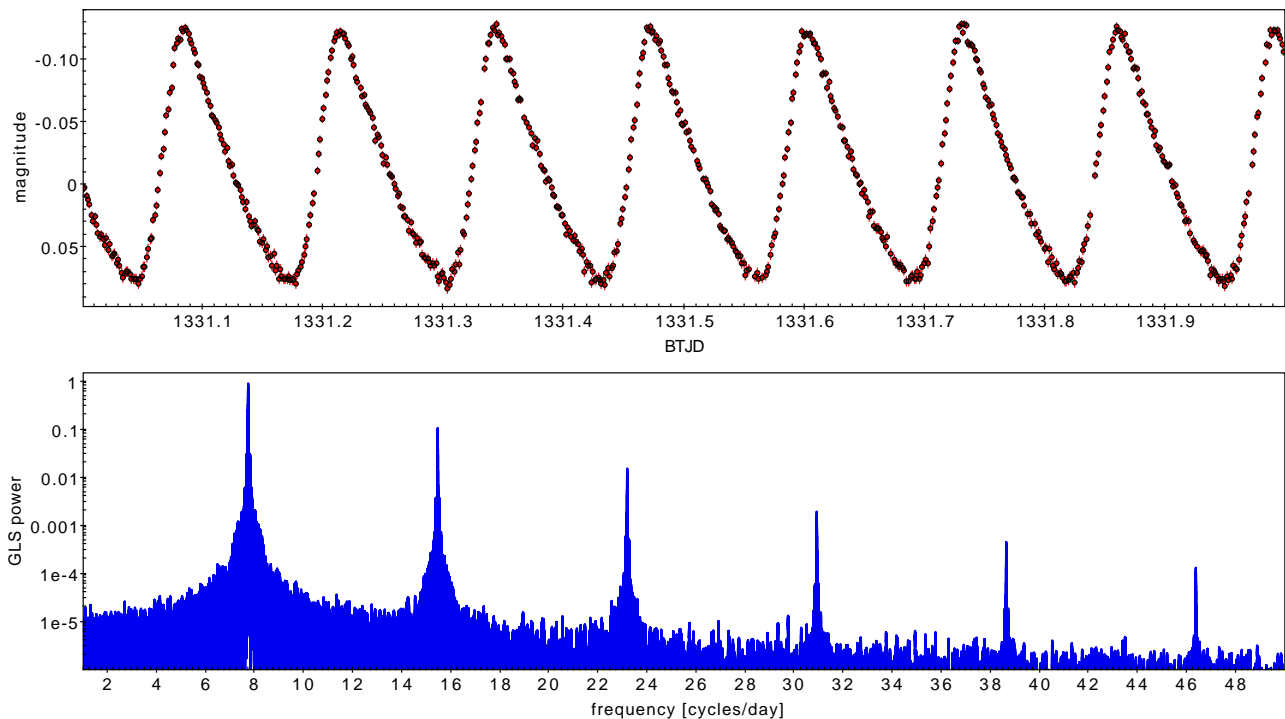


Fig. 1. TESS photometry of Chang 134 = TYC 9158-919-1. *Upper panel:* One-day section of the light curve from TESS sector 1. *Lower panel:* GLS periodogram of the whole light curve including nine TESS sectors, stitched together and filtered as explained in Sect. 3.

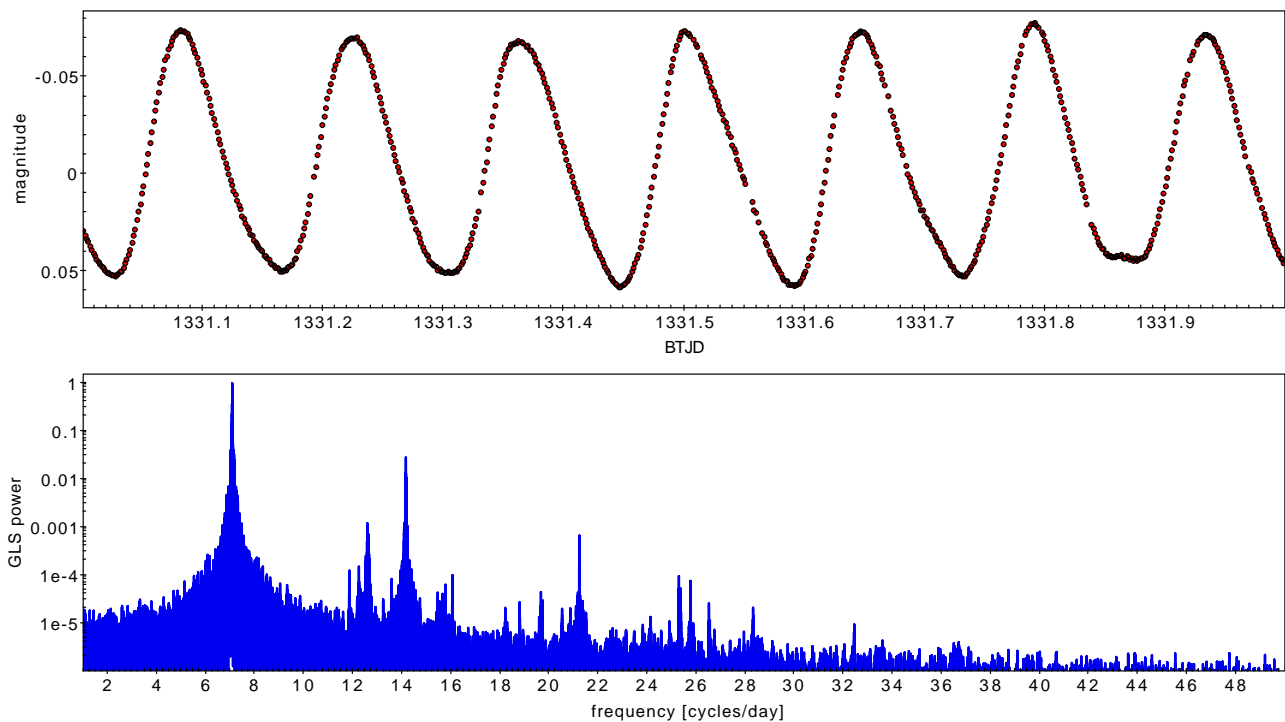


Fig. 2. TESS photometry of V393 Carinae = HD 66260. *Upper panel:* One-day section of the light curve from TESS sector 1. *Lower panel:* GLS periodogram of the whole light curve including 14 TESS sectors, stitched together and filtered as explained in Sect. 3.

where t_m is the median time of each orbit, set to minimize the correlations between the fit b_i parameters. The P_i periods must be fixed to their average values determined in the previous section in order to obtain meaningful phase shifts; for N harmonic components included, the number of free parameters is therefore $3 + 2N$. While N might in principle be arbitrarily large, for instance, when all the components that are even barely detectable

in the frequency spectrum are included, almost all the information on the phase shift is contained in the three most significant peaks, which sum up to $\gg 99\%$ of the total power. We therefore adopt $N = 3$ for our model by including the P_i constants from Eq. 3 and 4, implying nine free parameters for our fit. We verified this assumption by adding further harmonic terms as a test,

which resulted in statistically indistinguishable $O - C$ diagrams at the expense of a much more intensive computation.

We fit the model in Eq. 5 through a differential evolution Monte Carlo Markov chain algorithm (DE-MC; Ter Braak 2006), in which multiple MC chains are run in parallel and learn from each other how to converge to a global minimum in the parameter space, rather than running independently as in the classical approach. With respect to the least-squares techniques used by most previous works to fit harmonic series to light curves, DE-MC allowed us to obtain much more reliable error estimates on the final best-fit parameters because the posterior distribution takes any correlation between them into account. In order to increase the efficiency, we first fit only the oscillating term $\sum_i f_i$ of our model to each orbit with a Levenberg-Marquardt method (Moré 1978), to obtain reasonably good starting points for A_i and ϕ_i . Then we ran the DE-MC code, again orbit by orbit, to fit the full model with uninformative priors centered on the A_i , ϕ_i values found above, while the b_i parameters were initially set to zero. After 1 000 000 steps, the first 10% of the chain was discarded as burn-in phase and the posterior distributions of the nine fit parameters were examined to ensure that convergence was reached.

At this stage, when we plotted the residuals of the light curves after the best-fit model had been subtracted, we realized that a non-negligible number of outliers had escaped the previous filtering steps. These data points are mostly located close to momentum dumps of the spacecraft or at the beginning of each orbit when TESS cameras are not yet thermally stabilized. To deal with them, we discarded all the outliers at more than 5σ and fed the clipped light curves for a second run of the DE-MC fit, with the same configuration. The final best-fit parameters, especially the phases ϕ_i to which we are most interested in, are statistically consistent with those delivered from the first run, but usually with slightly smaller uncertainties.

Finally, the phase shifts ϕ_i , by our definition within the $[0, 1]$ interval, were converted into $O - C$ delays through a P_i factor. In principle, if the phase shifts were associated with independent pulsation modes and due solely to an LTTE, all the ϕ_i computed for the same orbit should result in the same $O - C$ value, within the measurement errors: $\phi_0 P_0 = \phi_1 P_1 = \phi_2 P_2$, and computing a weighted average $\langle \phi_i P_i \rangle$ would be the rigorous way to obtain the overall phase shift. This would also be a great opportunity to independently verify whether the LTTE model is the best explanation because different modes should yield the same $O - C$ (Hermes 2018). In our case, however, all the ϕ_i come from a single pulsation mode, and the harmonics do not carry additional information with respect to the fundamental frequency ν_0 , P_0 , where most of the spectral power lies: $\sigma(\phi_0) \ll \sigma(\phi_1) \ll \sigma(\phi_2)$ and thus $\phi_0 P_0 \simeq \langle \phi_i P_i \rangle$. For this reason, after confirming that the assumption above is true, we defined $\phi_0 P_0$ as our $O - C$. We associated the median epoch of the orbit t_m as a time stamp for each value as introduced above: $(O - C)(t_m) = \phi_0 \times P_0$. The resulting $O - C$ diagrams for Chang 134 and V393 Car are plotted in Fig. 3 and Fig. 4. The formal error bars are 1.5 s on average (range: 1.1-2.6 s) and 0.16 s (range: 0.14-0.19 s), respectively.

4. LTTE modeling

Even a quick look at both our $O - C$ diagrams (Fig. 3 and 4) reveals that neither can be reasonably fit by a straight line, that is, the resulting reduced χ_r^2 is $\gg 1$. The presence of a nonzero second derivative implies that the phase of the signal is evolving with time, and we can interpret this modulation by assuming that it is due to an LTTE from unseen companions. Following Kepler

et al. (1991), we parameterize our model as

$$O - C = (t_0 + \Delta P \cdot t) + \frac{1}{2} \frac{\dot{P}}{P} t^2 + \alpha \cos\left(\frac{2\pi t}{P_{\text{orb}}} + \varphi\right), \quad (6)$$

where t_0 is an arbitrary reference time, ΔP is the difference between the actual average pulsation period P and that estimated in Eq. 3 and 4, $\dot{P} = dP/dt$ accounts for a linear variation of P as a function of time, and α is the amplitude of an LTTE signal from a perturber on a circular⁶ orbit having an orbital period P_{orb} and with a phase φ .

From a physical point of view, the first term of Eq. 6 does not carry information because it represents just a change in the slope of the $O - C$ and does not imply any variation of the pulsation period. The second term, in the LTTE framework, represents a constant acceleration with respect to the barycenter of the system, possibly caused by a massive, perturbing body whose P_{orb} is much longer than our observing baseline (≈ 1000 d), such as stellar companions on very wide orbits. We should be aware here that several physical mechanisms other than LTTE can result in a $\dot{P} \neq 0$ term, including nonlinear interactions between different pulsation modes and stellar evolution effects. We return on this point in Section 4.2.

Last, the third, oscillating term of Eq. 6 is the LTTE modulation we are most interested in. As the first two terms play the role of a quadratic baseline in our fit, we make it more explicit by rewriting the model with $a_0 = t_0$, $a_1 = \Delta P$ and $a_2 = 0.5(\dot{P}/P)$,

$$(O - C)_{\text{quad}} = a_0 + a_1(t - t_m) + a_2(t - t_m)^2 + \alpha \cos\left(\frac{2\pi t}{P_{\text{orb}}} + \varphi\right), \quad (7)$$

where the median epoch of each orbit t_m has been subtracted from the time variable in order to minimize the correlations between a_0 , a_1 , and a_2 .

In order to confirm the uniqueness of our best-fit solution and the significance of the quadratic coefficient a_2 , we also performed a second fit to each data set by fixing $a_2 = 0$ in our model, that is, by imposing a linear baseline,

$$(O - C)_{\text{lin}} = a_0 + a_1(t - t_m) + \alpha \cos\left(\frac{2\pi t}{P_{\text{orb}}} + \varphi\right). \quad (8)$$

According to the Irwin (1952) model, for a circular orbit (eccentricity $e = 0$) and assuming that the perturbing body is much less massive than the star ($m_p \ll M_\star$), the amplitude of the LTTE signal is

$$\alpha = \frac{a \sin(i)}{c} \frac{m_p}{M_\star}, \quad (9)$$

where c is the speed of light, a is the orbital semimajor axis of the perturber and i is the inclination of its orbital plane with respect to the sky plane. In other words, when α and P_{orb} are measured from the $O - C$ data, the stellar mass is known (from Table 1) and a is derived from Kepler's laws, we can constrain the minimum mass of the perturber as $m_p \sin i$, with the same degeneracy on i as for the RV and astrometric techniques,

$$m \sin(i) = \alpha \times c \left(\frac{M_\star}{P_{\text{orb}}}\right)^{2/3} \left(\frac{G}{4\pi^2}\right)^{-1/3}. \quad (10)$$

⁶ Throughout this paper we assume a circular orbit as a simplifying hypothesis for our LTTE model, although a significant fraction of exoplanetary systems and binary stars are known to have nonzero eccentricity (Kim et al. 2018). This is justified by our need to avoid two additional free parameters (e and ω) and is further discussed in Section 5.

We started the fitting process by computing a GLS periogram on our $O - C$ diagrams to search for periodic modulations. For both targets, a single, well-defined peak stands out, at about 82 d and 1000 d for Chang 134 and V393 Car, respectively. We then fit our full LTTE model with both a quadratic and linear baseline (parameterized as in Eq. 7 and 8, respectively) on our $O - C$ diagrams through DE-MC, setting uninformative priors on all the five or six free parameters involved: a_0 , a_1 , a_2 , α , P_{orb} , and φ in the $(O - C)_{\text{quad}}$ model, and a_0 , a_1 , α , P_{orb} , and φ in the $(O - C)_{\text{lin}}$ model, and centering the boundaries of P_{orb} on the values previously found by GLS to speed up the convergence. As done at the harmonic analysis stage, after 1 000 000 steps, the first 10% of the chain was then discarded as burn-in phase, and we extracted the best-fit values and the associated errors of our parameters from their posterior distributions. All these values are reported in Table 2 for the four independent fits. The mass of the perturbing body $m_p \sin i$ was calculated as well as a derived parameter by propagating the relevant errors in Eq. 10.

4.1. Orbital solution for Chang 134

The best-fit $(O - C)_{\text{quad}}$ model for Chang 134 is overplotted on our $O - C$ in the upper panel of Fig. 3 as a solid cyan line, with the quadratic baseline $a_0 + a_1 t + a_2 t^2$ plotted as a dashed orange line. The resulting χ^2 of the residuals (lower panel of Fig. 3) is 56.7, with the reduced χ^2 being $\chi^2_{\text{red}} = \chi^2/\text{DOF} \approx 4.36$, where $\text{DOF} = 18 - 6 = 12$ are the degrees of freedom of our fit. It is worth noting that the best-fit value for a_2 is statistically consistent with zero (Table 2, second column), that is, we do not see any evidence of long-term LTTE effects because the derived \dot{P} is also consistent with zero. This is confirmed by the fact that the best-fit linear model $(O - C)_{\text{lin}}$ (Table 2, first column) yielded the same results within the error bars for all the fit parameters, with a virtually indistinguishable χ^2 (56.4 vs. 56.7). In other words, because the $(O - C)_{\text{quad}}$ model is not favored by our data, we hereafter adopt the results from the $(O - C)_{\text{lin}}$ fit.

The best-fit returned the amplitude of the LTTE term to be $\alpha = 6.11 \pm 0.65$ s (according to Eq. 6), and after propagating the errors through Eq. 9, we obtain a minimum mass of $m_p \sin i = 43.1 \pm 4.7 M_{\text{jup}}$ for the hypothetical companion. This is within the brown dwarf regime (13-80 M_{jup} ; Grieves et al. 2021).

4.2. Orbital solution for V393 Car

Unlike the case of Chang 134, the results from V393 Car fits are more difficult to interpret because the two models $(O - C)_{\text{quad}}$ and $(O - C)_{\text{lin}}$, while having a similar shape, led us to different orbital solutions. The two best-fit models are overplotted on our $O - C$ in the upper panel of Fig. 4 and 5 as a solid cyan line, respectively, with the linear and quadratic baseline $a_0 + a_1 t + a_2 t^2$ plotted as a dashed orange line.

While it is clear that at least an oscillating term is needed to fit the $O - C$ data, the inclusion of a quadratic term yields different parameters for the LTTE sinusoid: $P \approx 1071$ d with amplitude $\alpha \approx 107$ s for the $(O - C)_{\text{lin}}$ fit versus $P \approx 723$ d with amplitude $\alpha \approx 48$ s for the $(O - C)_{\text{quad}}$ fit. The discrepancy of a factor of ~ 2 in the α parameter translates into a similar ratio for the derived hypothetical companion masses: $m_p \sin i = 175.7 \pm 9.2 M_{\text{jup}}$, or $0.17 \pm 0.01 M_{\odot}$ (linear model) and $m_p \sin i = 102.0 \pm 5.3 M_{\text{jup}}$, or $0.10 \pm 0.01 M_{\odot}$ (quadratic model). We emphasize that for both scenarios, the minimum mass would be consistent with a cool

dwarf of spectral type M5V and M6V, respectively (Pecaut & Mamajek 2013).

A technique that is commonly employed for model selection problems like this is the evaluation of metrics such as the Akaike information criterion (AIC; Akaike 1974) or the Bayesian information criterion (BIC; Schwarz 1978). In the case of Gaussian distributions, the latter can be written as $\text{BIC} = \chi^2 + k \ln n$, where k is the number of free parameters and n is the number of data points. If applied literally to our problem, the BIC would overwhelmingly favor our $(O - C)_{\text{quad}}$ scenario ($\Delta\text{BIC} \gg 10$). Unfortunately, this result is distorted by the fact that the χ^2 of the residuals for both fits (lower panel of Fig. 4 and 5) is exceptionally high due to the extremely low formal error bars with respect to the systematic errors at play (on which we comment in Section 5): for the $(O - C)_{\text{quad}}$ fit, for instance, we obtained $\chi^2 = 8627$, with the reduced χ^2 being $\chi^2_{\text{red}} = \chi^2/\text{DOF} \approx 392$, where $\text{DOF} = 28 - 6 = 22$ are the degrees of freedom of our fit. This fact, and the very sparse phase sampling of our signal, prevents us from reaching a firm conclusion on the properties of this candidate companion, which will require further data to be confirmed and better constrained. New TESS observations of V393 Car are planned for Cycle 5, during four consecutive sectors (61-64; from January to May 2023), and again in Sector 68 (August 2023). Since the predictions from the $(O - C)_{\text{quad}}$ and $(O - C)_{\text{lin}}$ models will diverge by ~ 12 h by mid-2023, we expect that the extension of our analysis to the new TESS light curves will definitely be conclusive about the correct scenario.

As a side note, we could wonder whether the quadratic term we found when we assumed a quadratic baseline ($a_2 = 650 \pm 4$ ppm/s as fitted on our $O - C$ plane, translating into $\dot{P}/P \approx 5.5 \cdot 10^{-6} \text{ yr}^{-1}$) might be consistent with other non-LTTE mechanisms, as previously mentioned. Significant non-linear interactions between pulsating modes (Silvotti et al. 2018; Bowman et al. 2021) are not at play here because the spectral power outside the main pulsation mode and its harmonics is essentially negligible. On the other hand, the typical \dot{P}/P expected from evolutionary effects range from 10^{-9} to 10^{-7} yr^{-1} (Bregier & Pamyatnykh 1998; Xue et al. 2022), that is, it is much lower than our fitted value.

The same reasoning can be applied to Chang 134, for which we measure a nonsignificant quadratic term $a_2 = -2.2 \pm 7.5$ ppm/s corresponding to $\dot{P}/P \approx (-1.8 \pm 6.6) \cdot 10^{-8} \text{ yr}^{-1}$. Unlike V393 Car, this upper limit is still within the predictions for evolutionary effects. For instance, if we adopt $\dot{P}/P \approx 3 \cdot 10^{-9} \text{ yr}^{-1}$ (as measured on AE UMa by Xue et al. 2022), we obtain a total contribution on the $O - C$ of ~ 0.35 s over the full baseline of our observations (~ 1000 d), which is well below our current measurement error.

5. Discussion and conclusions

We applied the PT technique to two δ Scuti stars observed by TESS in a large number of sectors, detecting a periodic modulation on their $O - C$ that is consistent with the presence of companions in both cases: a BD ($m_p \sin i = 43.1 \pm 4.7 M_{\text{jup}}$) on a $P \approx 82$ d orbit around Chang 134, and a more massive body ($m_p \sin i \approx 0.10\text{-}0.17 M_{\odot}$) around V393 Car, whose orbital parameters are still not firmly constrained by the limited phase sampling of the signal. This double detection on the very first two targets analyzed by our project may appear to be very lucky. Still, the binary fraction of δ Scuti primaries as estimated by a previous PT search on Kepler data is rather high: $15.4 \pm 1.4\%$ (Murphy et al. 2018). In addition, unlike the quoted work, we

Table 2. Output parameters and associated errors for the best-fit LTTE models (Eq. 6) found for Chang 134 and V393 Car. For each of the four independent fits (i.e., linear and quadratic), we report the best-fit values and uncertainties of our parameters returned by their posterior distributions as a result of the DE-MC iterations.

	Chang 134	Chang 134	V393 Car	V393 Car
baseline	linear	quadratic	linear	quadratic
t_m [BJD _{TDB}]	1668.16969	1668.16969	2060.26634	2060.26634
a_0 [s]	0.17 \pm 0.35	0.19 \pm 0.99	-14.63 \pm 0.19	-68.22 \pm 0.26
a_1 [ppt]	1.4 \pm 1.2	1.9 \pm 1.8	205.25 \pm 0.23	448.3 \pm 0.14
a_2 [ppm/s]	0 (fixed)	-2.2 \pm 7.5	0 (fixed)	650.3 \pm 3.7
P_{orb} [days]	81.96 \pm 0.28	82.09 \pm 0.29	1071.5 \pm 1.0	724.7 \pm 2.0
ϕ_0	0.204 \pm 0.072	0.215 \pm 0.074	0.7485 \pm 0.0016	0.9081 \pm 0.0071
α [s]	6.11 \pm 0.65	6.99 \pm 0.66	107.25 \pm 0.09	47.96 \pm 0.17
$m_p \sin i$ [M_{jup}]	43.1 \pm 4.7	49.2 \pm 4.8	175.7 \pm 9.2	102.0 \pm 5.3
χ^2	56.7	56.4	17326	8627
χ_r^2	4.36	4.69	753	392

Notes. As discussed in Section 4, the adopted solution for Chang 134 is based on the linear model (first column), while for V393 Car, the data coverage is still insufficient to tell which model between $(O - C)_{\text{lin}}$ and $(O - C)_{\text{quad}}$ corresponds to the actual orbital solution.

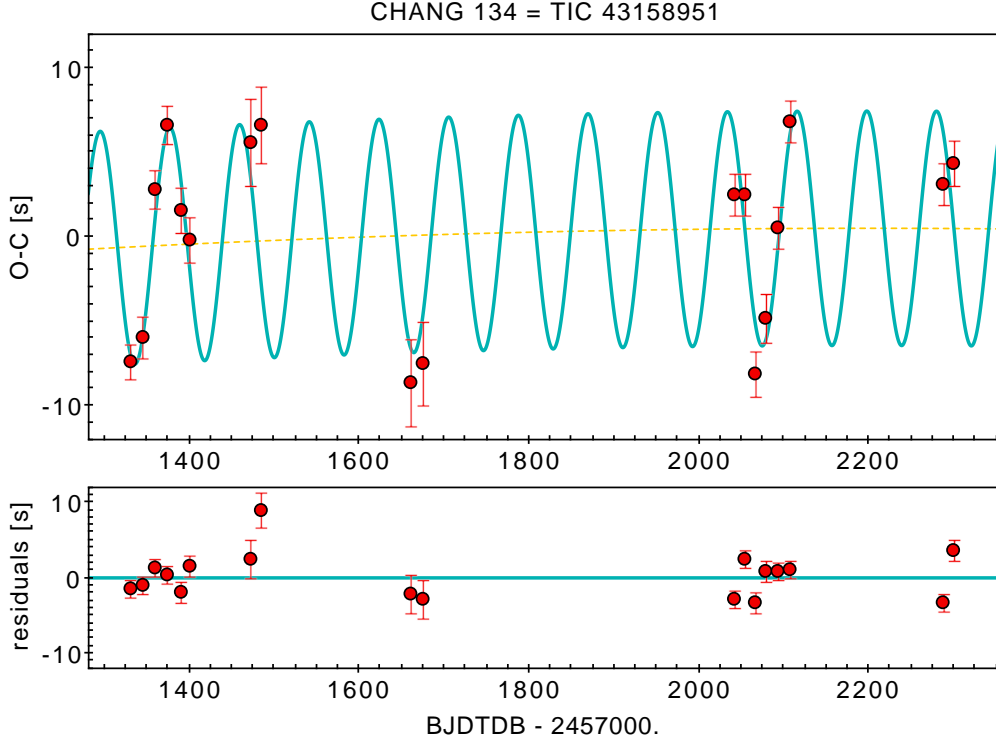


Fig. 3. Orbital solution for Chang 134. *Upper panel:* O-C diagram for the main pulsation mode of Chang 134 in seconds. The best-fit LTTE solution (including a quadratic trend) is overplotted as a continuous cyan line, and the quadratic baseline is plotted as a dashed orange line (see Section 3 for details). *Lower panel:* Residuals from the best-fit model in seconds.

initially restricted our sample in order to target only the most favorable stars in terms of sensitivity to LTTE signals. The overall binary fraction of A-type stars is estimated to be significantly larger than 50% by most authors (Duchêne & Kraus 2013), making our results less surprising. Any further statistical implication is prevented by the small size of our sample and by the heavy selection effects at play. As a side note, however, we mention that Borgniet et al. (2019) constrained the BD frequency within 2-3 au around AF stars to be below 4% (1σ) based on 225 targets observed with SOPHIE and/or HARPS, and that other authors hypothesized the presence of a brown dwarf desert extending to early-type stars (Murphy et al. 2018). This would make the

companion of Chang 134 an uncommon object, worthwhile to be followed up with more data and/or different techniques. The future TESS observations (at least five sectors of Cycle 5 are already scheduled, starting in March 2023) will also possibly help in constraining the eccentricity of the LTTE orbit, forced to zero in our analysis to avoid overfitting given our limited phase coverage and small number of $O - C$ points.

In addition to our results for these two specific stars, our analysis was based on an independent and improved implementation of the PT method (Murphy et al. 2014). It is also intended as a pilot study that is a prelude to a systematic search of LTTE companions around pulsating stars on a much larger scale, exploiting

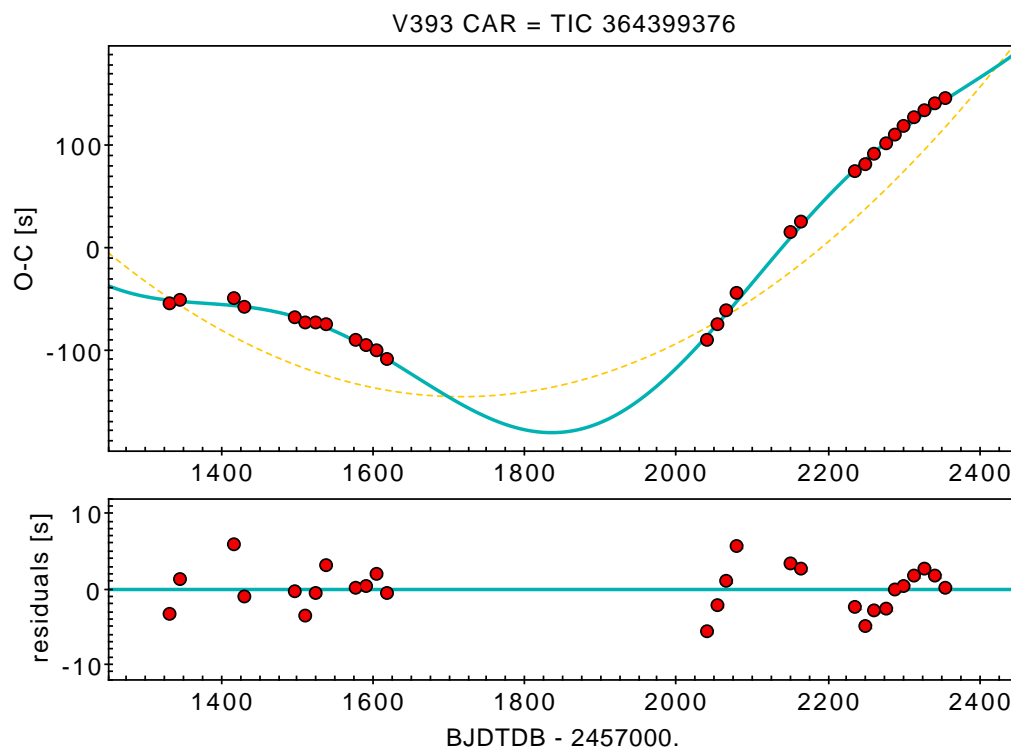


Fig. 4. Quadratic orbital solution for V393 Car. *Upper panel:* O-C diagram for the main pulsation mode of V393 Car in seconds. The best-fit LTTE solution with a quadratic baseline ($O - C$)_{quad} (Eq. 7) is overplotted as a continuous cyan line (see Section 3 for details). The quadratic baseline $a_0 + a_1t + a_2t^2$ is plotted separately as a dashed orange line. The nominal error bars (~ 0.16 s on average) are smaller than the point size. *Lower panel:* Residuals from the best-fit model in seconds.

the huge sample of δ Scuti targets that are and will be monitored through the availability of TESS FFIs at 10-minute cadence. The results for Chang 134, in particular, demonstrates that the detection of bodies in the substellar regime is perfectly feasible from TESS light curves, and that in some particularly favorable configuration, candidates with planetary masses ($m_p \sin i \lesssim 13 M_{\text{jup}}$) might be already within reach. A perturber with the same LTTE amplitude as was found on Chang 134 ($\alpha \approx 7$ s), for instance, but on a larger orbit at $P \approx 800$ d, would imply a companion with a mass of $\approx 2 M_{\text{jup}}$ detected at high significance.

On the other hand, our analysis highlighted several limiting factors that are worth discussing further. The first factor, largely self-evident in the case of V393 Car (Section 4.2), is related to the sparse sampling of the TESS light curves, an unavoidable consequence of its fixed scanning law (Ricker et al. 2015). Even for targets within or close to the CVZ at ecliptic latitudes $|\beta| \gtrsim 78^\circ$, that is, targets that are observed in up to 13 contiguous sectors, there is always a large gap every other year, which make the detection of signals at longer periods ($P \gtrsim 1$ year) difficult or ambiguous. Unfortunately, this is also the region in the parameter space where the PT technique is more sensitive to low-mass perturbers, owing to the Eq. 9 relation. As TESS is continuing its mission through extension phases, the accumulated data will mitigate this issue by filling out all or most of the orbital phases on the folded $O - C$ diagram.

A second, subtler limiting factor is the excess scatter in our $O - C$ data, as can be seen from the very high χ_r^2 values reported in Table 2 and discussed Section 4.2. Our residuals from the best-fit LTTE model have an rms of ~ 3 s in both fits, regardless of the average nominal error bars, which are about ten times lower on V393 Car than on Chang 134. The most plausible cause for this are systematic errors in the absolute calibration

of the time stamp. This issue has been anticipated by the TESS team, and in particular by the TESS Asteroseismic Science Consortium (TASC), who gave accurate timing requirements in the SAC/TESS/0002/6 document⁷, including RS-TASC-05: “[...] the time given for each exposure should be accurate over a period of 10 days to better than 1 second”. No requirement is given at longer timescales, however, and the TESS data release notes (DRN⁸) have reported systematic offsets in the time stamps for several sectors on the order of seconds, that is, consistent with the excess $O - C$ scatter we measured. While some of the reported offsets have been already corrected in subsequent update data releases, others are still waiting to be implemented. A ground-based campaign by von Essen et al. (2020) tried to independently confirm the absolute time calibration of TESS by comparing observations of a sample of eclipsing binaries in common, measuring a global offset of 5.8 ± 2.5 s; the errors of the measurements at individual epochs, however, are too large ($\gtrsim 10$ s) to confirm or disprove the systematic errors we see. We emphasize that offsets of a few seconds are usually completely negligible when investigating transiting exoplanets, but they are crucial in extending the sensitivity of the PT technique to planet-mass companions. An important outcome of a large-scale PT analysis of TESS data will allow us also to identify and correct these systematic errors by comparing the timing residuals of tens or hundreds of targets, following a self-calibration approach.

The same technique as applied in this work, and in general, the expertise gained through this project, will also help the scientific exploitation of PLATO (Rauer et al. 2014), for which the PT analysis could be a compelling case of ancillary science. Unlike TESS, no FFIs will be downloaded from PLATO during the

⁷ https://tasoc.dk/docs/SAC_TESS_0002_6.pdf

⁸ https://archive.stsci.edu/tess/tess_drn.html

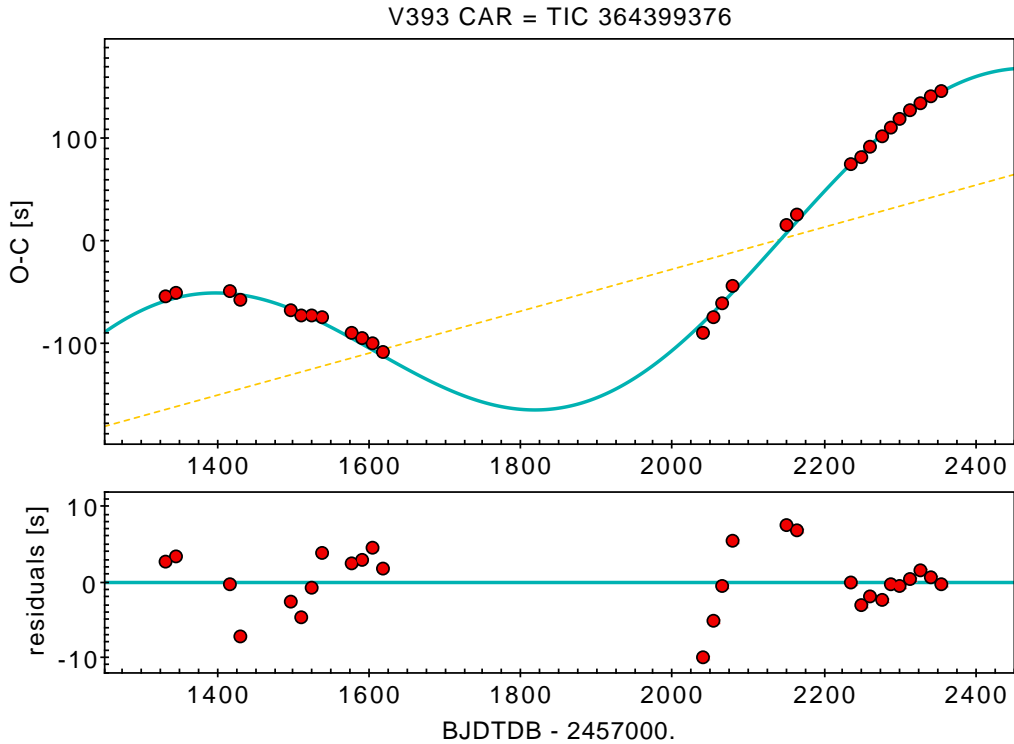


Fig. 5. Linear orbital solution for V393 Car. *Upper panel:* Same as Fig. 4, but with the best-fit LTTE solution with a linear baseline $(O - C)_{\text{lin}}$ (Eq. 8). The linear baseline $a_0 + a_1 t$ is plotted separately as a dashed orange line. *Lower panel:* Residuals from the best-fit model in seconds.

nominal observing phase, and no stars earlier than F5 are to be included in the main target samples, which are focused on transit search around solar-type stars (Montalto et al. 2021). Nevertheless, about 8% of the PLATO science data rate will be allocated to the General Observer (GO) program through ESA calls open to the whole astrophysical community. Any δ Scuti star (and, more in general, pulsating star) allocated as GO within a long-pointing field (Nascimbeni et al. 2022) would result in a mostly uninterrupted light curve on a baseline of two to four years, with a cadence⁹ and photometric precision far better than what is achieved by TESS, overcoming the sparse phase sampling affecting the latter. Even more important, the time stamps of each PLATO data point will be accurate within 1 s in an absolute sense by formal scientific requirement because of the specifically designed calibration processes that also include the monitoring of a preselected set of detached eclipsing binaries (Nascimbeni et al. 2022).

Acknowledgements. The authors wish to thank the referee, Dr. Roberto Silvotti, for the valuable and fruitful comments and suggestions which significantly improved our manuscript. This research has made use of the SIMBAD database (operated at CDS, Strasbourg, France; Wenger et al. 2000), the VARTOOLS Light Curve Analysis Program (version 1.39 released October 30, 2020, Hartman & Bakos 2016), TOPCAT and STILTS (Taylor 2005, 2006). Valerio Nascimbeni and Giampaolo Piotto recognize support by ASI under program PLATOASI/INAF agreements 2015-019-R.1-2018.

Note added in proof. After the acceptance of this paper, we have been contacted by Dr. D. Hey who let us know that he found a similar orbital solution for V393 Car using the *maelstrom* code (Hey et al. 2020). In particular, his results suggest that the linear-baseline model yields a better fit the timing data.

⁹ The nominal cadence of the “normal” PLATO cameras will be 25 s, i.e., a factor of about 5 shorter than the TESS standard cadence (Rauer et al. 2014).

References

- Ahlers, J. P., Barnes, J. W., & Myers, S. A. 2019, *AJ*, 158, 88
 Akaike, H. 1974, *IEEE Transactions on Automatic Control*, 19, 716
 Anders, F., Khalatyan, A., Queiroz, A. B. A., et al. 2022, *A&A*, 658, A91
 Antoci, V., Cunha, M. S., Bowman, D. M., et al. 2019, *MNRAS*, 490, 4040
 Auvergne, M., Bodin, P., Boisnard, L., et al. 2009, *A&A*, 506, 411
 Axelsen, R. A. 2014, *jaavso*, 42, 292
 Bailer-Jones, C. A. L., Rybizki, J., Fouesneau, M., Demleitner, M., & Andrae, R. 2021, *AJ*, 161, 147
 Balona, L. A. & Dziembowski, W. A. 2011, *MNRAS*, 417, 591
 Balona, L. A. & Evers, E. A. 1999, *MNRAS*, 302, 349
 Barceló Forteza, S., Moya, A., Barrado, D., et al. 2020, *A&A*, 638, A59
 Barclay, T., Pepper, J., & Quintana, E. V. 2018, *ApJS*, 239, 2
 Barlow, B. N., Dunlap, B. H., & Clemens, J. C. 2011a, *ApJ*, 737, L2
 Barlow, B. N., Dunlap, B. H., Clemens, J. C., et al. 2011b, *MNRAS*, 414, 3434
 Black, D. C. & Scargle, J. D. 1982, *ApJ*, 263, 854
 Borgniet, S., Lagrange, A. M., Meunier, N., et al. 2019, *A&A*, 621, A87
 Borucki, W. J., Koch, D., Basri, G., et al. 2010, *Science*, 327, 977
 Bowman, D. M. 2017, *Amplitude Modulation of Pulsation Modes in Delta Scuti Stars*
 Bowman, D. M., Hermans, J., Daszyńska-Daszkiewicz, J., et al. 2021, *MNRAS*, 504, 4039
 Bowman, D. M. & Kurtz, D. W. 2018, *MNRAS*, 476, 3169
 Breger, M. 2000, in *Astronomical Society of the Pacific Conference Series*, Vol. 210, *Delta Scuti and Related Stars*, ed. M. Breger & M. Montgomery, 3
 Breger, M. & Pamyatnykh, A. A. 1998, *A&A*, 332, 958
 Chang, S.-W., Protopapas, P., Kim, D.-W., & Byun, Y.-I. 2013, *The Astronomical Journal*, 145, 132
 Charbonneau, D., Brown, T. M., Latham, D. W., & Mayor, M. 2000, *ApJ*, 529, L45
 Collier Cameron, A., Guenther, E., Smalley, B., et al. 2010, *MNRAS*, 407, 507
 Cui, K., Liu, J., Yang, S., et al. 2019, *MNRAS*, 489, 5513
 Cutri, R. M., Skrutskie, M. F., van Dyk, S., et al. 2003, *VizieR Online Data Catalog*, II/246
 Duchêne, G. & Kraus, A. 2013, *ARA&A*, 51, 269
 Eastman, J., Siverd, R., & Gaudi, B. S. 2010, *PASP*, 122, 935
 Fausnaugh, M., Morgan, E., Vanderspek, R., et al. 2021, *PASP*, 133, 095002
 Gaia Collaboration, Brown, A. G. A., Vallenari, A., et al. 2018, *A&A*, 616, A1
 Gaia Collaboration, Brown, A. G. A., Vallenari, A., et al. 2021, *A&A*, 649, A1
 Gaia Collaboration, Vallenari, A., Brown, A. G. A., et al. 2022, *arXiv e-prints*, arXiv:2208.00211
 Garcia, J. R., Busso, V. A., & Ferrero Sosa, G. 2001, *jaavso*, 30, 44

- Grievess, N., Bouchy, F., Lendl, M., et al. 2021, *A&A*, 652, A127
- Guzik, J. A. 2021, *Frontiers in Astronomy and Space Sciences*, 8, 55
- Hartman, J. D. & Bakos, G. Á. 2016, *Astronomy and Computing*, 17, 1
- Hartman, J. D., Bakos, G. Á., Buchhave, L. A., et al. 2015, *AJ*, 150, 197
- Hasanzadeh, A., Safari, H., & Ghasemi, H. 2021, *MNRAS*, 505, 1476
- Helt, B. E. 1984, *A&AS*, 56, 457
- Henry, G. W., Marcy, G. W., Butler, R. P., & Vogt, S. S. 2000, *ApJ*, 529, L41
- Hermes, J. J. 2018, *Handbook of Exoplanets*, 787–796
- Herrero, E., Morales, J. C., Ribas, I., & Naves, R. 2011, *A&A*, 526, L10
- Hey, D. R., Montet, B. T., Pope, B. J. S., Murphy, S. J., & Bedding, T. R. 2021, *AJ*, 162, 204
- Hey, D. R., Murphy, S. J., Foreman-Mackey, D., et al. 2020, *AJ*, 159, 202
- Høg, E., Fabricius, C., Makarov, V. V., et al. 2000, *A&A*, 355, L27
- Howell, S. B., Sobek, C., Haas, M., et al. 2014, *PASP*, 126, 398
- Irwin, J. B. 1952, *ApJ*, 116, 211
- Jenkins, J. M., Twicken, J. D., McCauliff, S., et al. 2016, in *Society of Photo-Optical Instrumentation Engineers (SPIE) Conference Series*, Vol. 9913, *Software and Cyberinfrastructure for Astronomy IV*, ed. G. Chiozzi & J. C. Guzman, 99133E
- Kepler, S. O., Winget, D. E., Nather, R. E., et al. 1991, *ApJ*, 378, L45
- Kim, C. H., Kreiner, J. M., Zakrzewski, B., et al. 2018, *ApJS*, 235, 41
- Mayor, M. & Queloz, D. 1995, *Nature*, 378, 355
- Mints, A. & Hekker, S. 2017, *A&A*, 604, A108
- Montalto, M., Borsato, L., Granata, V., et al. 2020, *MNRAS*, 498, 1726
- Montalto, M., Piotto, G., Marrese, P. M., et al. 2021, *A&A*, 653, A98
- Moré, J. J. 1978, in *Lecture Notes in Mathematics*, Berlin Springer Verlag, Vol. 630, 105–116
- Moya, A., Zuccarino, F., Chaplin, W. J., & Davies, G. R. 2018, *ApJS*, 237, 21
- Murphy, S. J., Barbara, N. H., Hey, D., Bedding, T. R., & Fulcher, B. D. 2020, *MNRAS*, 493, 5382
- Murphy, S. J., Bedding, T. R., & Shibahashi, H. 2016, *The Astrophysical Journal*, 827, L17
- Murphy, S. J., Bedding, T. R., Shibahashi, H., Kurtz, D. W., & Kjeldsen, H. 2014, *MNRAS*, 441, 2515
- Murphy, S. J., Moe, M., Kurtz, D. W., et al. 2018, *MNRAS*, 474, 4322
- Murphy, S. J. & Shibahashi, H. 2015, *MNRAS*, 450, 4475
- Nardiello, D., Borsato, L., Piotto, G., et al. 2019, *MNRAS*, 490, 3806
- Nascimbeni, V., Piotto, G., Börner, A., et al. 2022, *A&A*, 658, A31
- Paparo, M., Szeidl, B., & Mahdy, H. A. 1988, *Ap&SS*, 149, 73
- Pecaut, M. J. & Mamajek, E. E. 2013, *ApJS*, 208, 9
- Pojmanski, G. 2002, *Acta Astron.*, 52, 397
- Queiroz, A. B. A., Anders, F., Chiappini, C., et al. 2020, *A&A*, 638, A76
- Queiroz, A. B. A., Anders, F., Santiago, B. X., et al. 2018, *mnras*, 476, 2556
- Rainer, M., Borsa, F., Pino, L., et al. 2021, *A&A*, 649, A29
- Rauer, H., Catala, C., Aerts, C., et al. 2014, *Experimental Astronomy*, 38, 249
- Ricker, G. R., Winn, J. N., Vanderspek, R., et al. 2015, *Journal of Astronomical Telescopes, Instruments, and Systems*, 1, 014003
- Schneider, J. 2005, in *Astronomical Society of the Pacific Conference Series*, Vol. 335, *The Light-Time Effect in Astrophysics: Causes and cures of the O-C diagram*, ed. C. Sterken, 191
- Schofield, M., Chaplin, W. J., Huber, D., et al. 2019, *ApJS*, 241, 12
- Schwarz, G. 1978, *Annals of Statistics*, 6, 461
- Shibahashi, H. & Kurtz, D. W. 2012, *MNRAS*, 422, 738
- Shibahashi, H., Kurtz, D. W., & Murphy, S. J. 2015, *MNRAS*, 450, 3999
- Silvotti, R., Schuh, S., Janulis, R., et al. 2007, *Nature*, 449, 189
- Silvotti, R., Schuh, S., Kim, S. L., et al. 2018, *A&A*, 611, A85
- Smith, J. C., Stumpe, M. C., Van Cleve, J. E., et al. 2012, *PASP*, 124, 1000
- Southworth, J. 2021, *Universe*, 7, 369
- Sozzetti, A. 2005, *PASP*, 117, 1021
- Stassun, K. G., Oelkers, R. J., Paegert, M., et al. 2019, *AJ*, 158, 138
- Sterken, C. 2005, in *Astronomical Society of the Pacific Conference Series*, Vol. 335, *The Light-Time Effect in Astrophysics: Causes and cures of the O-C diagram*, ed. C. Sterken, 3
- Stumpe, M. C., Smith, J. C., Van Cleve, J. E., et al. 2012, *PASP*, 124, 985
- Taylor, M. B. 2005, in *Astronomical Society of the Pacific Conference Series*, Vol. 347, *Astronomical Data Analysis Software and Systems XIV*, ed. P. Shopbell, M. Britton, & R. Ebert, 29
- Taylor, M. B. 2006, in *Astronomical Society of the Pacific Conference Series*, Vol. 351, *Astronomical Data Analysis Software and Systems XV*, ed. C. Gabriel, C. Arviset, D. Ponz, & S. Enrique, 666
- Temple, L. Y., Hellier, C., Albrow, M. D., et al. 2017, *MNRAS*, 471, 2743
- Ter Braak, C. J. F. 2006, *Statistics and Computing*, 16, 239
- VanderPlas, J. T. 2018, *ApJS*, 236, 16
- von Essen, C., Lund, M. N., Handberg, R., et al. 2020, *AJ*, 160, 34
- Wenger, M., Ochsenbein, F., Egret, D., et al. 2000, *A&AS*, 143, 9
- Xue, H.-F., Niu, J.-S., & Fu, J.-N. 2022, *arXiv e-prints*, arXiv:2208.09158
- Zechmeister, M. & Kürster, M. 2018, *GLS: Generalized Lomb-Scargle periodogram*

Appendix A: O-C data tables

Appendix B: Detected frequencies

Table A.1. $O - C$ data points, best-fit models, and residuals for Chang 134.

BJD _{TDB} -2457000.	$O - C$ [s]	$\sigma(O - C)$ [s]	$(O - C)_{\text{lin}}$ model	$(O - C)_{\text{lin}}$ residuals	$(O - C)_{\text{quad}}$ model	$(O - C)_{\text{quad}}$ residuals
1331.92359	-7.438	1.068	-6.108	-1.330	-6.022	-1.415
1345.90832	-5.963	1.198	-5.058	-0.904	-4.998	-0.964
1360.60338	2.809	1.122	1.510	1.298	1.574	1.235
1375.00044	6.625	1.101	6.235	0.389	6.288	0.336
1390.56269	1.500	1.381	3.572	-2.072	3.571	-2.071
1401.41733	-0.206	1.291	-1.552	1.346	-1.603	1.396
1473.17464	5.535	2.578	3.383	2.152	3.223	2.312
1484.59180	6.586	2.316	-2.045	8.631	-2.253	8.839
1660.82652	-8.612	2.526	-6.003	-2.608	-6.403	-2.208
1675.51285	-7.523	2.504	-4.268	-3.255	-4.614	-2.909
2042.19462	2.504	1.243	5.634	-3.129	5.442	-2.937
2054.87251	2.432	1.233	0.210	2.222	-0.032	2.465
2065.98714	-8.098	1.382	-4.555	-3.543	-4.765	-3.333
2079.35797	-4.880	1.406	-5.615	0.735	-5.701	0.820
2093.48079	0.471	1.232	-0.462	0.934	-0.423	0.894
2107.49034	6.839	1.251	5.656	1.182	5.709	1.129
2287.53230	3.071	1.236	6.014	-2.943	6.356	-3.285
2300.70057	4.346	1.289	0.490	3.856	0.779	3.566

Notes. The columns list the time stamp in BJD_{TDB} (Eastman et al. 2010) minus a constant, the $O - C$ value and its error $\sigma(O - C)$ as evaluated by the pipeline described in Section 3, the best-fit model with a linear baseline $(O - C)_{\text{lin}}$ (Eq. 8) and its residuals, and the best-fit model with a quadratic baseline $(O - C)_{\text{quad}}$ (Eq. 7) and its residuals. The unit of all columns except for the first one is seconds.

Table A.2. $O - C$ data points, best-fit models, and residuals for V393 Car.

BJD _{TDB} -2457000.	$O - C$ [s]	$\sigma(O - C)$ [s]	$(O - C)_{\text{lin}}$ model	$(O - C)_{\text{lin}}$ residuals	$(O - C)_{\text{quad}}$ model	$(O - C)_{\text{quad}}$ residuals
1331.91976	-54.412	0.154	-56.976	2.564	-51.019	-3.392
1345.90080	-50.762	0.149	-53.998	3.236	-52.057	1.295
1415.83631	-50.206	0.170	-49.765	-0.440	-56.092	5.886
1430.69212	-58.366	0.151	-51.050	-7.316	-57.290	-1.076
1497.33248	-67.522	0.159	-64.881	-2.640	-67.171	-0.350
1510.38967	-73.668	0.153	-68.905	-4.762	-70.194	-3.474
1523.23291	-74.095	0.156	-73.198	-0.897	-73.549	-0.546
1538.50182	-74.948	0.194	-78.679	3.731	-78.030	3.081
1576.10597	-91.162	0.159	-93.498	2.335	-91.222	0.059
1589.91972	-96.422	0.150	-99.251	2.828	-96.753	0.330
1604.82852	-101.071	0.186	-105.545	4.474	-103.061	1.990
1617.98105	-109.424	0.162	-111.117	1.692	-108.865	-0.558
2041.24344	-89.695	0.160	-79.666	-10.028	-84.105	-5.589
2053.84041	-75.611	0.158	-70.408	-5.203	-73.458	-2.153
2066.69227	-61.262	0.139	-60.657	-0.605	-62.354	1.091
2079.92126	-44.973	0.164	-50.340	5.367	-50.738	5.764
2150.46034	14.949	0.143	7.536	7.412	11.516	3.432
2164.39670	26.042	0.167	19.136	6.906	23.356	2.685
2235.00659	75.437	0.157	75.446	-0.009	77.893	-2.456
2248.25195	82.000	0.150	85.183	-3.182	86.914	-4.913
2261.29517	92.533	0.152	94.410	-1.877	95.404	-2.871
2276.00083	101.932	0.182	104.336	-2.404	104.51	-2.586
2287.40641	111.230	0.157	111.655	-0.424	111.26	-0.037
2300.50082	119.058	0.150	119.617	-0.558	118.69	0.362
2313.64933	127.478	0.159	127.108	0.370	125.83	1.640
2326.99985	135.568	0.165	134.168	1.400	132.80	2.762
2340.08852	141.165	0.144	140.530	0.634	139.40	1.761
2353.92851	146.208	0.144	146.632	-0.423	146.18	0.020

Notes. The columns list the time stamp in BJD_{TDB} (Eastman et al. 2010) minus a constant, the $O - C$ value and its error $\sigma(O - C)$ as evaluated by the pipeline described in Section 3, the best-fit model with a linear baseline $(O - C)_{\text{lin}}$ (Eq. 8) and its residuals, and the best-fit model with a quadratic baseline $(O - C)_{\text{quad}}$ (Eq. 7) and its residuals. The unit of all columns except for the first one is seconds.

Table B.1. Significant GLS frequencies detected for Chang 134.

ν [c/d]	P [days]	GLS power	notes
7.72651415	0.12942447	0.8961	ν_0
15.45302830	0.06471223	0.1057	$2\nu_0$
23.17954244	0.04314149	0.0153	$3\nu_0$
30.90605512	0.03235611	0.0019	$4\nu_0$
38.63256381	0.02588489	4.48e-4	$5\nu_0$
46.35909289	0.02157074	1.34e-4	$6\nu_0$
54.08564236	0.01848919	4.35e-5	$7\nu_0$
61.81213065	0.01617805	1.24e-5	$8\nu_0$
69.53870051	0.01438048	3.68e-6	$9\nu_0$

Notes. The columns list the frequency ν in cycles per day, the corresponding period P in days, the GLS power of the peak, and the identification of the mode or harmonics when available. The list is sorted by decreasing GLS power. See Section 3 for details.

Table B.2. Significant GLS frequencies detected for V393 Car.

ν [c/d]	P [days]	GLS power	notes
7.07738170	0.14129519	0.9655	ν_0
14.15476341	0.07064759	0.0275	$2\nu_0$
21.23214517	0.04709840	0.0011	$3\nu_0$
12.58288531	0.07947302	6.65e-4	ν_1
12.23921459	0.08170458	1.47e-4	—
11.85401165	0.08435962	1.22e-4	—
16.05643640	0.06228032	9.84e-5	—
25.28532371	0.03954863	9.33e-5	$2\nu_1?$
13.57492256	0.07366524	8.19e-5	—
25.75951070	0.03882061	7.45e-5	—
19.66029065	0.05086394	4.37e-5	$\nu_0 + \nu_1$
18.79289737	0.05321159	2.68e-5	—
26.51035806	0.03772110	2.58e-5	—
18.20796573	0.05492101	2.06e-5	—
28.30950295	0.03532382	2.06e-5	$4\nu_0$
20.85998893	0.04793866	1.99e-5	—
20.52339810	0.04872487	1.95e-5	—
24.12779695	0.04144597	1.32e-5	—
32.43606157	0.03082988	9.28e-6	—

Notes. The columns list the frequency ν in cycles per day, the corresponding period P in days, the GLS power of the peak, and the identification of the modes or harmonics when available. Here ν_1 marks the secondary pulsation mode identified at ~ 12.58 cycles per day, unlike Eq. 4, where it marks the second most significant peak (corresponding to $2\nu_0$ in the present table). The list is sorted by decreasing GLS power. See Section 3 for details.